research papers

A novel monochromator for experiments with ultrashort X-ray pulses

Maria Brzhezinskaya,[a] Alexander Firsov,[a] Karsten Holldack,[b]* Torsten Kachel,[b] Rolf Mitzner,[b] Niko Pontius,[b] Jan-Simon Schmidt,[a] Mike Sperling,[b] Christian Stamm,[b] Alexander Föhlisch[b] and Alexei Erko[a]

[a]Institute for Nanometer Optics and Technology, Helmholtz-Zentrum Berlin für Materialien und Energie, Albert-Einstein-Strasse 15, Berlin 12489, Germany, and [b]Institute for Methods and Instrumentation in Synchrotron Radiation Research, Helmholtz-Zentrum Berlin für Materialien und Energie, Albert-Einstein-Strasse 15, Berlin 12489, Germany.
E-mail: karsten.holldack@helmholtz-berlin.de

Aiming at advancing storage-ring-based ultrafast X-ray science, over the past few years many upgrades have been undertaken to continue improving beamline performance and photon flux at the Femtoslicing facility at BESSY II. In this article the particular design upgrade of one of the key optical components, the zone-plate monochromator (ZPM) beamline, is reported. The beamline is devoted to optical pump/soft X-ray probe applications with 100 fs (FWHM) X-ray pulses in the soft X-ray range at variable polarization. A novel approach consisting of an array of nine off-axis reflection zone plates is used for a gapless coverage of the spectral range between 410 and 1333 eV at a designed resolution of $E/\Delta E = 500$ and a pulse elongation of only 30 fs. With the upgrade of the ZPM the following was achieved: a smaller focus, an improved spectral resolution and bandwidth as well as excellent long-term stability. The beamline will enable a new class of ultrafast applications with variable optical excitation wavelength and variable polarization.

Keywords: femtosecond X-ray pulses; storage ring; elliptical undulators; slicing; diffractive optics; reflection zone plates; time-resolved X-ray spectroscopy.

1. Introduction

Ordering phenomena in solids like charge, orbital and spin order as well as electronic structure phenomena in molecular and highly correlated electron systems evolve on sub-picosecond timescales (Stamm *et al.*, 2007; Gavrila *et al.*, 2009; Boeglin *et al.*, 2010; Holldack *et al.*, 2010). It has been demonstrated that ultrashort pulses of synchrotron radiation in the soft X-ray spectral range with variable polarization are a proven tool for exploring ultrafast dynamics in matter on a nanoscale especially the topic of ultrafast magnetization dynamics on relevant length and timescales (Wietstruk *et al.*, 2011; Radu *et al.*, 2011; Eschenlohr *et al.*, 2013).

The Femtoslicing facility at BESSY II (Khan *et al.*, 2006) is a unique set-up for studying ultrafast dynamics with soft X-ray pulses of ∼100 fs pulse duration and variable linear and circular polarization. It was installed in 2004 as the first undulator-based slicing facility and is still, as far as we know, the only storage-ring-based facility yielding soft X-ray pulses in the soft X-ray range (250–1400 eV) of ∼100 fs (FWHM) duration and variable polarization.

Slicing facilities (Schoenlein *et al.*, 2000; Ingold *et al.*, 2007) inherently generate intrinsic synchronization of femtosecond

X-ray and femtosecond laser pulses, which is the most salient advantage of storage-ring-based slicing compared with similar experiments at free-electron lasers (FELs) without seeding (Yu, 1991). The simple fact that X-ray pulses generated by 'slicing' are always extracted from the same electron bunch results in a very low charge fluctuation (no shot noise) and hence in an excellent intensity stability of the X-ray probe pulses. However, the extraordinary temporal stability of storage-ring-based sources of ultrashort (temporarily incoherent) X-ray pulses is only possible at the expense of photon flux. Therefore, a high-transmission optics preserving the temporal length of the pulses and the brilliance of the beam is a mandatory ingredient of such a facility.

Reflection zone plates (RZPs), which consist of elliptical zones fabricated as laminar grating structures on a mirror surface, have been proven to effectively monochromatize a soft X-ray beam and to focus it at photon energies below 1400 eV at high transmittance up to 20% (Erko *et al.*, 2008; 2010). However, RZPs are highly chromatic and they can be designed only for one photon energy.

Here, we alleviate the problem by using a novel approach: a reflection zone-plate array (RZPA) that covers a large bandwidth while preserving pulse shape and flux. We report a

successful implementation of a novel monochromator based on a RZPA specifically designed for experiments with ultrashort soft X-ray pulses at slicing and HHG sources (*e.g.* Popmintchev *et al.*, 2010) that usually suffer from low average photon flux.

2. The quest for an ideal optics

The Femtoslicing facility is installed in the high-beta straight section H11/D6 of the storage ring BESSY II equipped with a UE56 elliptical undulator as a 'radiator' that emits 100 fs pulses at 6 kHz repetition rate. The UE56/1 is an APPLE-II undulator (minimum gap 16.6 mm) and covers the range from 110 eV (first harmonic) up to 2 keV (fifth harmonic) with full polarization control (Bahrdt, 2012). The initial beamline set-up consisted of a plane-grating monochromator (PGM) equipped with 150, 400 and 1200 lines mm^{-1} gratings. The PGM beamline, being one of the workhorses at BESSY II (Weiss *et al.*, 2001; Kachel *et al.*, 2007), consists of five optical elements that ensure highest resolution and tiny focus but its transmittance in the soft X-ray range is only 1%. Initial slicing experiments (Holldack *et al.*, 2005; Stamm *et al.*, 2007) have been successfully performed at this beamline but the number of detected 100 fs photons was only 10^3–10^4 photons s^{-1} (0.1% bandwidth)$^{-1}$ at 1 kHz, *i.e.* 1–10 photons pulse^{-1}. Although the PGM beamline is invaluable for static and picosecond pump–probe spectroscopy, it is less useful for slicing operation owing to the transmittance drawback mentioned above.

One route to increase the photon flux is to reduce the number of reflections. Heimann *et al.* (2006) selected a solution for the slicing beamline at the Advanced Light Source that is based on a variable-line-spacing grating of high transmittance surrounded by three additional focusing mirrors. Here, the optic has to perform both separation of photons from the sliced bunch and monochromatization. In our case the (angular) separation part (Khan *et al.*, 2006) is already performed upstream by front-end slits, such that a single dispersive optical element at only one reflection is possible. Single-element monochromators based on toroidal gratings (HETGM monochromator, *e.g.* Woodruff, 1995) or spherical gratings (Warwick *et al.*, 1995) could be used as a further alternative to match the high flux requirement.

Avoiding complex substrates and taking into account that a tailored RZP optics can now be easily manufactured on plane blanks within few weeks by our in-house facilities, it was decided to go for the RZP design described below. Moreover, plane substrates as used in our case show significant better slope deviations of 0.5 µrad (r.m.s.) and a micro-roughness of better than 0.1 nm (r.m.s.) as measured with a white-light interferometer (magnification 20× and 50×). Both values can barely be

achieved for toroidal surfaces (Siewert, 2013).

Giving up the flexibility of a PGM design (Weiss *et al.*, 2001), a design study suggested that an RZP (Aristov *et al.*, 1988; Basov *et al.*, 1994; Wilhein *et al.*, 1997) can well accommodate the case of time-resolved X-ray circular dichroism (XMCD) and resonant soft X-ray diffraction (RSXD), where a moderate spectral resolution of $E/\Delta E \simeq 100$–1000 is sufficient but any single photon really counts. However, owing to the chromatic drawback of RZPs, any photon energy to be addressed would need a special lens design.

To this end, after first tests with three lenses (Fe, Ni, Co), a prototype high-flux monochromator based on six RZPs covering the range from 546 to 1206 eV was built in 2008 (Erko *et al.*, 2010) and implemented into the BESSY Femtoslicing set-up and operated in parallel with the existing PGM beamline until 2010. However, since this first zone-plate monochromator (ZPM) set-up at that time was only foreseen as a test stand for a prototype RZP design, the system had certain mechanical limitations regarding stability, energy range and accuracy of the photon energy control. Since a major upgrade of Femtoslicing in 2010 the facility has been supporting variable wavelength from UV-MIR in the pump laser (FEMTOSPEX, 2013) that requires a smaller laser spot and forced us to accommodate the X-ray probe spot size. Therefore, the goal of the new conceptual design described below was to alleviate the beamline's stability issues, extend the energy range (gapless) and decrease the focal spot size.

3. Design of reflection zone plates

3.1. Overview

A schematic diagram of an off-axis reflection zone plate (Aristov *et al.*, 1988; Wilhein *et al.*, 1997; Niemann, 1995) imprinted as a projection on a totally reflecting mirror surface is shown in Fig. 1. The structure, being a laminar grating of variable line spacing in two dimensions, is capable of imaging the source by diffraction onto a certain distance R_2 along the optical axis, acting as both a dispersive and focusing optical element. However, owing to the high chromaticity of a zone plate, *i.e.* the dependence of the focal length on wavelength,
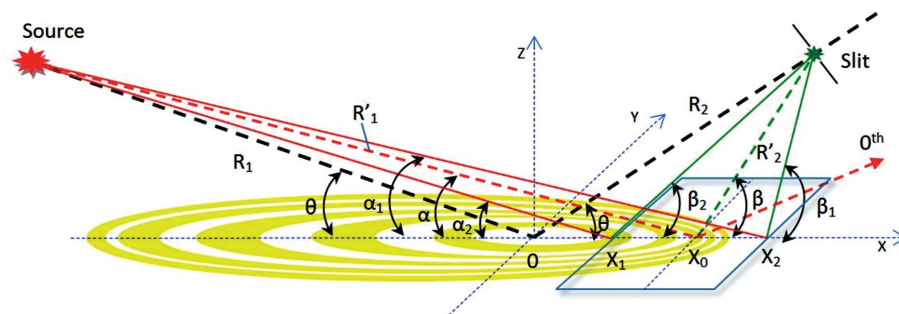
Figure 1
Layout of an off-axis reflection zone plate and explanation of the corresponding parameters (see text). The blue rectangle marks the used section as an off-center cut-out of the full elliptical lens structure. R_1 and R_2 are the distances between source and focal plane to the center of the zone plate, respectively, while R'_1 and R'_2 are the corresponding distances to the center of the off-axis part of the lens (blue rectangle).

different energies are focused on different positions along the optical axis.

3.2. Design and monochromator properties of a single RZP

As depicted in Fig. 1, the full elliptical lens structure is not used but only an off-axis section as marked by the blue rectangle. Recalling the fact that a zone plate is a hologram of a point source, one knows that the radiation from the off-center section is focused in the same manner as for the full lens but at high dispersion owing to the higher average line density. In addition, the specular reflex (zero order of the grating) can be nicely separated and, most valuable for monochromatization, a slit in a plane perpendicular to the optical axis can be applied for energy selection. The calculation below is based on the fact that each infinitesimal part of the lens has to fulfil the grating equation. An RZP design starts with an optimization of the angle of incidence α maximizing the figure of merit $R(\alpha)\sin(\alpha)$, where R is the reflectivity. A value of $\alpha = 2°$ is chosen for a gold surface.

In a second step we need to select a desired resolution and how it is linked to the parameters in Fig. 1. An RZP disperses the incident beam as emitted by the source S along the optical axis. The same phenomenon is used in variable-line-spacing gratings in one dimension (Heimann *et al.*, 2006) to provide spectral dispersion. The focal distance $F(\lambda)$ along the axis depends on the radiation wavelength according to

$$F(\lambda) = F(\lambda_0)\,\lambda_0/\lambda, \tag{1}$$

where $F(\lambda_0)$ is the focal distance at the design wavelength λ_0 of the lens. All other energies are dispersed along the focal plane not being transmitted through the slit. Considering an infinitesimal part in the center of the off-axis part of the lens, the linear angular dispersion in the plane perpendicular to the optical axis can be locally calculated using the regular grating formula,

$$d(\cos\alpha - \cos\beta) = m\lambda, \tag{2}$$

where d is the grating period, α is the grazing angle of incidence on the RZP (off-axis) area, β is the grazing diffraction angle and m is the order of diffraction. After a simple transformation and setting $m = 1$ for the first order, we can derive the first-order's angular dispersion of the grating in the middle of the working area at the position X_0,

$$\frac{\Delta\beta}{\Delta\lambda} = \frac{1}{d\sin\beta}, \tag{3}$$

where $\Delta\lambda$ is the wavelength change upon $\Delta\beta$. Taking the angular dispersion available from (3) one can calculate the wavelength resolution in the case where a slit of size Δh in the focal plane exists,

$$\frac{\lambda}{\Delta\lambda} = \frac{R'_2\lambda}{\Delta h\,d\sin\beta} \qquad \text{if} \qquad \Delta h \geq \Delta S(R'_2/R'_1), \tag{4}$$

where Δh is the slit width, R'_1 and R'_2 are the corresponding source–grating and grating–focus distances, respectively, and ΔS is the vertical source size, which is $\Delta S \simeq 57\ \mu m$ (FWHM) for the high-beta straight section in the regular user electron

optics of BESSY II (Kuske, 2013). A geometrical demagnification factor $M = R'_2/R'_1 = 5.2$, chosen to accommodate the laser spot in our case, limits the minimum slit width to $\Delta h = 11\ \mu m$. The reciprocal energy dispersion D^{-1} in the focal plane as easily derived from (4) then reads

$$D^{-1} = \frac{\Delta E}{\Delta h} = \frac{E^2 d\sin\beta}{R'_2 hc}. \tag{5}$$

By combining equations (2), (3) and (4) and considering now also all other diffraction orders m, it is straightforward to calculate the local period d of the optical element that satisfies the requested focusing condition in the diffraction order m along the two-dimensional structure,

$$d = \frac{|m|\lambda}{\sin\alpha}\left\{\left[1 + \cot^2\alpha + \left(\frac{R'_2}{\Delta h}\frac{\Delta\lambda}{\lambda}\right)^2\right]^{1/2} - \frac{m}{|m|}\cot\alpha\right\}. \tag{6}$$

Using equation (7) we can determine the missing design parameters of the RZP according to Fig. 1: the angle between the optical axis and the surface θ as well as the distances R_1 and R_2 between the center of the RZP, the source and the image, respectively,

$$\theta = \tan^{-1}\left[\frac{R'_1\sin\alpha + R'_2\sin\beta}{R'_1\cos\alpha + R'_2\cos\beta}\right], \tag{7}$$

$$R_1 = \frac{R'_1\sin\alpha}{\sin\theta} \qquad \text{and} \qquad R_2 = \frac{R'_2\sin\beta}{\sin\theta}. \tag{8}$$

Margins of the off-axis working area that are related to these values are indicated in Fig. 1 as X_1 and X_2 coordinates with the corresponding diffraction angles (β_1, β_2) and input angles (α_1, α_2) as well as their corresponding local grating periods available from equations (6) and (3).

Once these parameters are determined, the lens design is unambiguously established for one certain focal length $F(\lambda)$ at the wavelength λ.

4. Temporal elongation of X-ray pulses

Since the beamline is supposed to support ultrafast experiments, pulse elongation by the diffractive structure is an important issue. Pulse stretching caused by an optical grating is proportional to the number of illuminated grating lines times the wavelength. The maximum number of grooves N_{max} that can be illuminated while preserving a certain pulse length can thus be expressed as

$$N_{max} = t_{pulse}/t_\lambda, \tag{9}$$

where Δt_{pulse} is the specified X-ray pulse elongation, $\Delta t_\lambda = \lambda/c$ is the time delay and c is the speed of light. At a photon energy of 713 eV at the Fe L-edge, Δt_λ is $\sim 5.8 \times 10^{-18}$ s. Hence, with equation (9), and a specified maximum pulse elongation of 30 fs, it follows that $N_{max} = 5200$, a value that directly defines the maximum aperture of the lens and the highest possible energy resolution. For the parameters of the lenses described below in the energy range 410–1333 eV, the average grating

periods are $d \simeq 15$–25 µm, values that limit the lengths of the RZPs to 80 mm in each case.

Table 1
Design parameters for the two different Fe-RZPs.

$\lambda/\Delta\lambda$	α (°)	β (°)	Θ (°)	R'_1 (mm)	R'_2 (mm)	X_1 (mm)	X_0 (mm)	X_2 (mm)
500	2	2.12	2.0187	26500	5080	205	245	285
2000	2	2.50	2.0807	26500	5080	987	1027	1067

5. Reflection zone-plate array

5.1. General layout

The inherent feature of zone plates, *i.e.* the focal distance depends on wavelength, limits the useful bandwidth of a monochromator being based on them, unless slit or sample travel with wavelength (no fix-focus condition). The other option is to add additional surrounding mirrors compensating for this drawback at the expense of flux. Here, we followed the route to keep the flux advantage and to alleviate the band-width limit problem by using an array of RZPs. Under certain conditions a large energy range can be covered in this way. The current design as depicted in Fig. 2 consists of nine lenses that enable a working range from 410 to 1333 eV at moderate spectral resolutions of $E/\Delta E = 500$ or, in one case, $E/\Delta E = 2000$.

The science-driven design energies of each individual RZP were set according to the following rules:

(i) In the case of K-edges (N, O) the design energy is directly set to the K-absorption edge.

(ii) In the case of L-edges (Mn, Fe, Co, Ni) the average energy between L_3 and L_2 absorption is used.

(iii) In the case of M-edges (rare-earth elements) the average energy between the M_4 and M_5 absorption edges is chosen as a design value.

One special lens (labeled Fe^{HR}) in Fig. 2 was manufactured to support higher resolution ($E/\Delta E = 2000$) for test purposes.
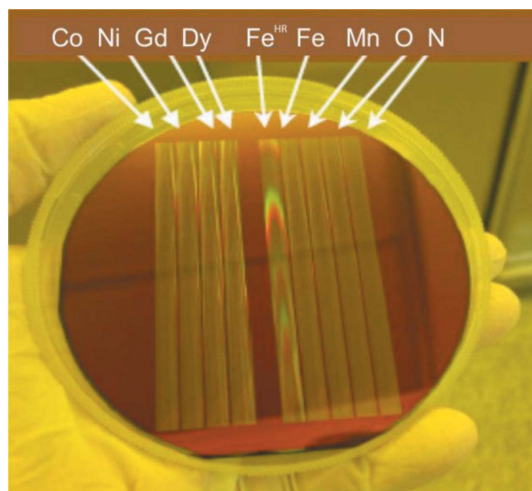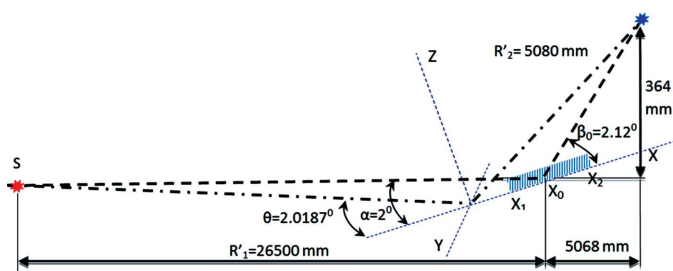

Figure 2
Reflection zone-plate array as designed for the new ZPM beamline at the Femtoslicing facility. The view is towards downstream from the source, the high-energy lenses (Co, Ni, Gd, Dy) are on the left side and separated by a gap of 5 mm from the low-energy lens group: Fe, Mn, O and N. The Fe^{HR} lens (or Fe 2000) as designed for higher resolution generates a different diffraction pattern in the visible caused by another average line spacing. The substrate is super-polished 10 mm-thick Si at 100 mm diameter coated with gold.

In this case we accept a larger pulse elongation of 120 fs according to equation (9).

In order to support pump–probe experiments with small laser focus, a geometry of highest possible demagnification ($M = 5.2$) was chosen as shown in Fig. 3. The RZPA operates at $\alpha = 2°$ grazing incidence at a distance of 26.5 m from the source and the deflection angle in the center X_0 of the off-axis working area of the lens is $\beta_0 = 2.12°$.

As an example, two sets of lens-specific optical parameter settings for the two Fe-RZPs are compared in Table 1. This reveals the fact that the higher the lens resolution the more off-center (X_0) is the used active part of the elliptical zone plate.

A simulation of the monochromator performance of RZPs was performed in greater detail using the ray-tracing program *RAY* developed at BESSY (Schäfers, 2008). Expected focal sizes, energy resolution, influence of slope errors and surface roughness, as well as required alignment accuracies, were predicted. As an example, the intensity distribution in the focal plane of the RZP for the Fe 500 lens is depicted in Fig. 4(a). The monochromator energy resolution is 1.43 eV in the case of a 20 µm vertical slit but it decreases along the dispersion plane down to ∼3 eV if the energy is >10 eV off (Fig. 4a). A typical dispersion in this particular geometry is $D = 71$ eV mm^{-1}. The results demonstrate that a spectral resolution of at least $E/\Delta E \simeq 300$ is available, a few percent off the design energy. A corresponding change of the resolution for the Fe 2000 (Fe^{HR}) lens is plotted in Fig. 4(b). We also see that, even if the resolution is worse off the central energy, XAS, RSXD and XMCD at the two L-edges is possible in both cases but at the expense of either spectral resolution or significant pulse elongation at higher resolution (Fig. 4b). The spectral blurring occurring off the design energy is a consequence of unavoidable energy dispersion along the (4.1° grazing) optical axis. By translating the lens or the slit longitudinally according to equation (1), the design resolution can be preserved during

Figure 3
Sketch of the 'as built' set-up of all RZPs designed for $E/\Delta E = 500$. In the case of the Fe 2000 lens, β_0 and some of the parameters had to be changed to accommodate the same focus position, as listed in Table 1.
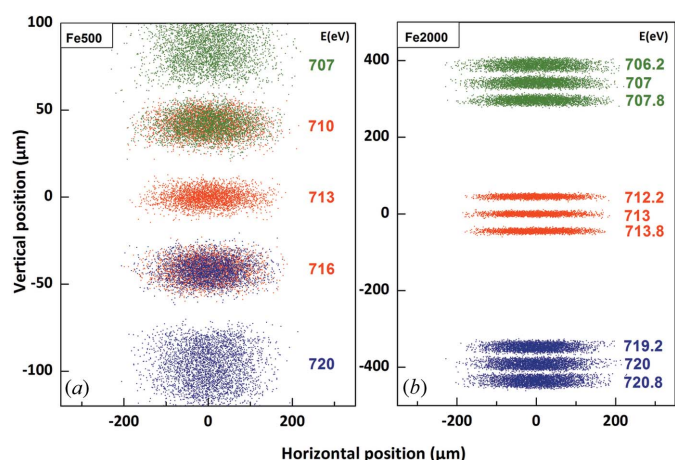
Table 2
Parameters of the low-energy RZP set.

Element	$\lambda/\Delta\lambda$	β_0 (°)	E (eV)	d_0 (µm)	D^{-1} (eV mm^{-1})	Δt_{pulse} (fs)
N	500	2.12	410	41.6	41.1	30
O	500	2.12	543	31.4	54.4	30
Mn	500	2.12	644	26.5	64.5	30
Fe 500	500	2.12	713	23.9	71.4	30
Fe 2000	2000	2.50	713	5.0	14.9	120

Table 3
Parameters of the high-energy RZP set.

Element	$\lambda/\Delta\lambda$	β_0 (°)	E (eV)	d_0 (µm)	D^{-1} (eV mm^{-1})	Δt_{pulse} (fs)
Co	500	2.12	786	21.7	78.7	30
Ni	500	2.12	861	19.8	86.2	30
Gd	500	2.12	1221	14.0	122.6	30
Dy	500	2.12	1333	12.8	133.6	30

pitch drives (changing α) within a larger range up to a few 100 eV. In practical experiments, however, longitudinal travel has not been performed so far since it causes a temporal delay in the arrival of the X-ray pulse and a corresponding shift of time-zero in pump–probe experiments.

To account for groove depth effects, explained further below, the RZPs were sorted into two sets: one set consisted of five low-energy (410–715 eV) RZPs and the other set consisted of four high-energy (786–1333 eV) lenses. The specifications of these RZPs are summarized in Tables 2 and 3 for the two different groups already shown above in Fig. 2.

Tables 2 and 3 nicely reveal a beauty of the design that the energy dispersion, albeit by chance, in units of (eV mm^{-1}), is almost exactly $E/10$, meaning that 10 µm in the dispersion plane corresponds to $E/1000$ for all RZPs except the Fe 2000 lens. In any event the design resolution is achieved at ∼20 µm slit width.

Table 4
Variation of the line density and dispersion for the Fe 500 lens along its surface.

$X - X_0$ (mm)	α (°)	β_0 (°)	d (µm)	L (lines mm^{-1})	D^{-1} (eV mm^{-1})
−40	2.00	2.10	28.79	34.73	85.9
0	2.00	2.12	23.86	41.91	71.3
40	2.00	2.13	20.31	49.23	60.1

5.2. Variable line density and dispersion

In order to demonstrate the variable line spacing along the lens, the line period d was calculated using equation (6) and the parameters from Table 1 for the energy and resolution values as chosen before. Using trigonometric ratios, d and L were calculated in the center of the RZPs as well as at ±40 mm off at a total length of $\Delta X = X_2 - X_1 = 80$ mm (see Table 4). It was found that L and d only weakly change spatially along the lens. The main reason for this is that the RZPs are located relatively far from both the source and the image. However, in practical usage one has to be aware of this effect especially if the lens is vertically not fully illuminated or if α and β become considerably larger than grazing.

5.3. Laminar groove depth and efficiency

The diffraction efficiency of each individual RZP considerably oscillates with the groove depth depending on energy as plotted in Figs. 5(a) and 5(b), a consequence of the path difference of individual wave trains reflected from the top and the bottom of the laminar grating structure. Here, the *REFLEC* software (Schäfers & Krumrey, 1996) as developed at Helmholtz-Zentrum Berlin (HZB) to design and optimize VUV/X-ray optical elements and beamlines was employed to determine the optimum groove depth for each lens. The results are presented in Figs. 5(a) and 5(b) for the low- and

Figure 4
Ray-tracing results for the RZP designed for XMCD experiments at the Fe $L_{2,3}$-edges at a resolution of $E/\Delta E = 500$ (a) and at $E/\Delta E = 2000$ (b) at 713 eV. The available resolution off the central design energy declines (a) to $E/\Delta E = 300$ at the two different L-edges in a plane perpendicular to the optical axis and (b) to $E/\Delta E = 1000$ for the Fe 2000 lens.
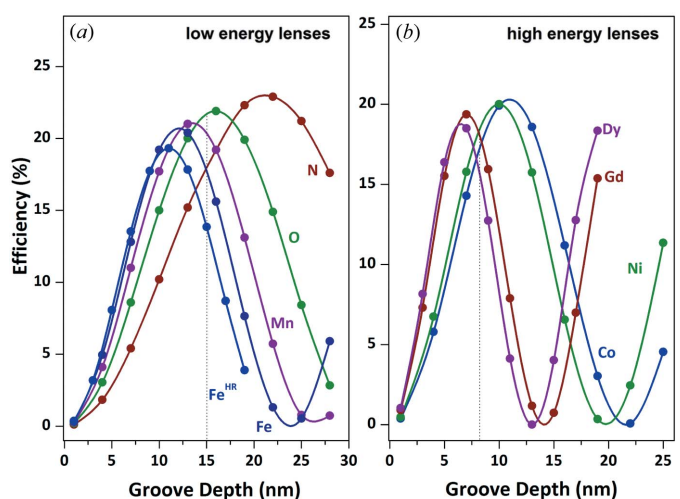
Figure 5
Diffraction efficiency of individual lenses for the low-energy (a) and the high-energy case (b). Dotted lines mark groove depths of 15 nm and 8.3 nm, respectively, selected as optimum settings for the current RZPA.
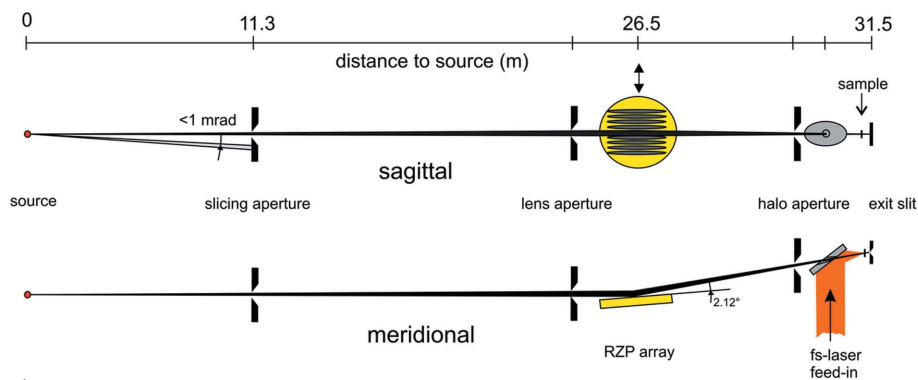
Figure 6
Optical layout of the ZPM beamline after the upgrade in 2012. In order to select a certain lens and energy range, the optical element (RZPA, yellow) is traveled horizontally perpendicular to the optical axis driven by a stepping motor. A special laser feed-in (orange) is an inherent part of the approach enabling pump–probe experiments with variable pump wavelength from UV to MIR at large numerical aperture.

angular divergence of undulator radiation at given photon energy is (Wiedemann, 1998)

$$\sigma_r' \simeq \frac{1}{\gamma}\left(\frac{1+K^2/2}{2Nk}\right)^{1/2}, \qquad (10)$$

where K is the deflection parameter, k is the harmonic number, γ is E/mc^2 and N is the number of periods (in our case $N = 30$). For $K = 1$ and $k = 1$ one finds $\sigma_r' = 50\ \mu$rad, leading to a footprint of $\sim$3 mm FWHM on the RZP. That is, a horizontal width of 5 mm is large enough to accept the on-axis radiation cone from the radiator. At a lens length of 80 mm, as given by the pulse elongation requirement, the vertical acceptance is 2.8 mm at 26.5 m. In order to achieve a focus of 150 μm (FWHM), a demagnification of $R_1'/R_2' = 5.2$ was chosen, a value that represents a trade-off between optimum lens design and geometrical constraints to handle the experimental stations at the beamline's back end. The final design is depicted in Fig. 6. Apertures at 11.3 m (front-end slits) are used to discriminate femtosecond and picosecond photons in the 'slicing' mode, where regular photons from the radiator are being deflected off by an angular bump in the electron beam and finally dumped into one of the front-end slits (Khan *et al.*, 2006). The beamline layout itself has no exit slit which has to be a part of the user experiment. However, in order to achieve the RZP's theoretical resolution limits, a slit has to be placed exactly at R_2'.

high-energy lens group, respectively. Although each individual lens would actually require an individual groove depth for optimum efficiency, Figs. 5(a) and 5(b) suggest that a depth of 15 nm for the high-energy lens set and 8.3 nm for the low-energy set lead to optimized efficiencies for all lenses. Hence, only these two different groove depths for the two groups of lenses have been correspondingly used during manufacturing employing a masking technique (see Appendix A). Simulations for our case have further shown that there is almost no spatial efficiency variation along the RZPs at $\alpha = 2°$. The efficiencies averaged over the entire lens range from 13.9% (for Fe 2000) to 21.6% for the oxygen (O) lens, as indicated by dotted lines in Fig. 5. All lenses with $E/\Delta E = 500$ show an efficiency variation of only $\sim$12%.

We further note here that RZPs at 2° grazing incidence fully preserve the elliptical polarization of the photon beam as is well known from other grazing-incidence optics.

## 6. Beamline approach and its realisation

Aiming at the highest possible flux, the beamline should accept the full central cone radiation pattern from the undulator. For large distances to the source (in our case 26.5 m) the

The special purpose of the beamline to support ultrafast experiments requires a very special layout that was improved compared with the existing test set-up before. A general side view of the set-up as built in November 2012 is depicted in Fig. 7. A cubic ultrahigh-vacuum vessel containing the RZPA is located at 26.5 m away from the source and mounted onto a rigid granite block that consists of two separated parts. The upper part that holds the monochromator vessel can slide perpendicular to the beam along grinded rails in the lower
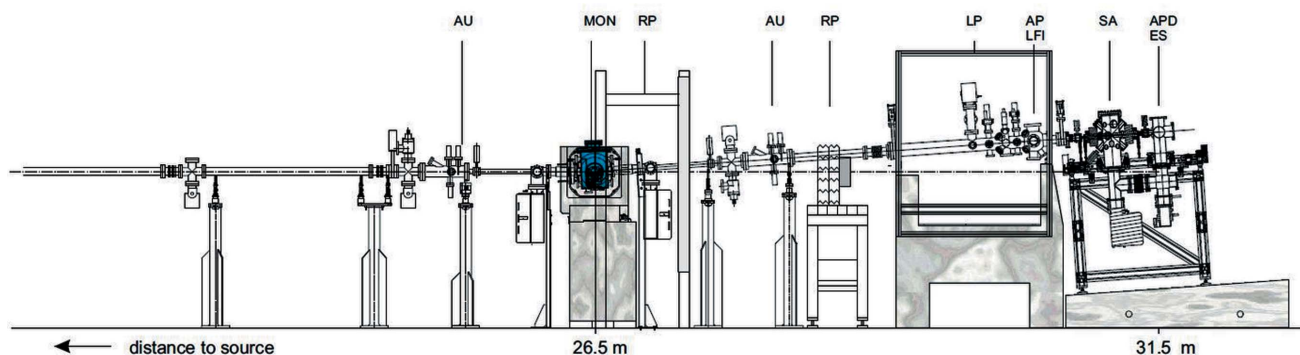
Figure 7
Mechanical design of the new ZPM beamline. The monochromator vessel containing the RZPs is highlighted in light blue. Gray shaded areas indicate the massive composite granite blocks beneath key components as the lens mount and the laser feed line. Legend: AU, aperture units; MON, monochromator; RP, radiation protection; LP, laser protection; LFI, laser feed line; SA, sample; APD/ES, exit slit and avalanche photodiode (or other detectors).
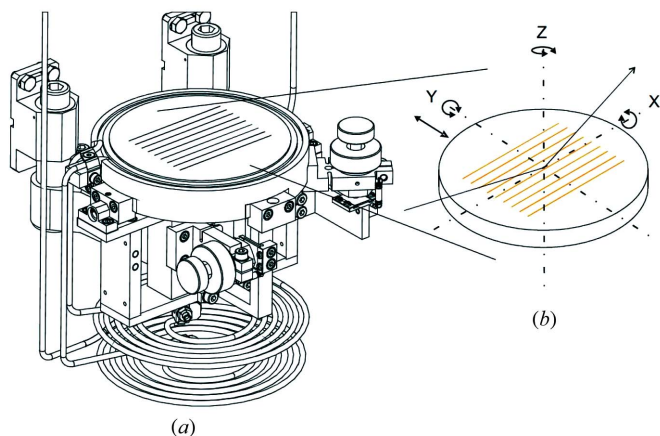
Figure 8
(a) Assembly drawing of the in-vacuum lens support with piezo motors, gears and cooling pipes. (b) Sketch of a lens array and axis definition: X, roll; Y, pitch; Z, yaw.

base part at a precision of <10 μm (repeatability). Users can select the lens of interest driving this axis.

Two heavy blocks of composite granite act as a rigid base for the laser feed line set-up as well as a wedge-shaped block (4°) for different experimental chambers (see Fig. 7).

The RZPA is installed in the vessel at 26.5 m and embedded in a water-cooled rigid copper base (see Fig. 8) which can be rotated in-vacuum along two axes, X (roll) and Z (yaw), by in-vacuum piezo drives that are spring-pretensioned. The pitch drive around the Z-axis is realised by rotating the whole vacuum vessel using a mechanical-bearing direct-drive rotary stage. Both pitch and translation perpendicular to the beam are controlled either by optical or magnetic encoders. All rotations cover a range of ±1° at 0.5 arcsec precision and the translation has a stroke of 60 mm at <10 μm repeatability.

The arm length R'_2 behind the monochromator is 5080 mm (see Figs. 3 and 8) and the distance between the last valve and the focus is ∼45 cm. For time-resolved XMCD and XAS measurements it is mandatory to place the detector with 20, 40 and 100 μm slits in front at the focal plane. For RSXD measurements the scattering chamber is longitudinally shifted such that the focus is on the sample rather than on the slit.

The 100 fs X-ray and the 50 fs pump laser pulses are merged ∼800 mm upstream of the sample by a 3-inch-diameter broad band metal mirror with a 1.5 mm hole in the center to ensure a collinear propagation of both beams.

7. Commissioning results

The photon distribution along the dispersion plane behind the RZPA was initially characterized employing BESSY II's focus chamber, where X-ray spots can be imaged using a P43 phosphor and a lens-coupled CCD detector with 3 μm resolution. The measured focal spot sizes (FWHM) are 160 μm horizontally and 20, 40 and 100 μm vertically, corresponding to the slit width (slits are removed in the case of the maps in Fig. 9). At a demagnification of $M = 5.2$, a value of the horizontal spot size of 145 μm (10% less than measured) is predicted according to the reasonable estimate that it should be ∼$2.35M(\varepsilon\beta)^{1/2}$, where $\varepsilon = 6\pi$ nm rad is the design emittance and β is the beta function in the high-beta straight sections of BESSY II. The 10% deviation can likely be explained by slight modifications of BESSY II's electron optic (Kuske, 2013) in 2012.

Color-coded X-ray intensity maps obtained in the focal plane from all RZPs are depicted in Fig. 9. In the current case the radiator (UE56/1) was set such that the fifth harmonic was always at the design energy of the RZP. As expected, the lens performs a horizontal focusing at this energy, while the seventh harmonic appears as a blurred bar at the bottom ∼4 mm off horizontal focus. The specular reflex is not shown here but it is only 10 mm below the first-order focus. The measured pattern can be explained as follows: the dovetail shape above the focus is red-shifted radiation from the fifth harmonic. The two side-lobes below the focus arise from the sixth harmonic that is emitted only off-axis. The stripe at the bottom is the seventh harmonic that always has the same distance.

To explain this, let the energy be E at harmonic N of the undulator beam and the energy difference between two subsequent odd harmonics $2E/N$. Then the distance Δh_{odd} between them in the dispersion plane is
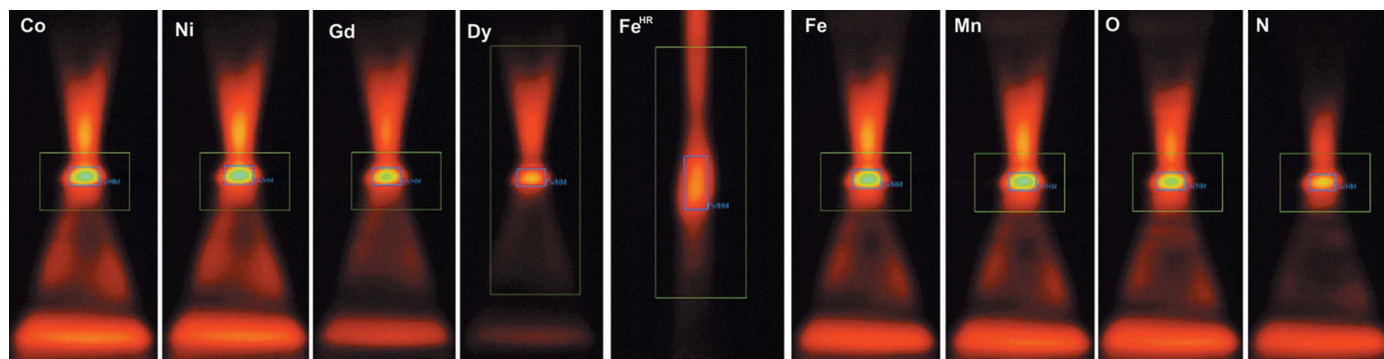
Figure 9
Focal plane images on a P43 phosphor screen with the photon energy set to the corresponding design values at the fifth harmonic of the UE56/1. Except for the high-resolution Fe lens (Fe 2000 = Fe^{HR}), the seventh harmonic appears as a blurred stripe at the bottom, but always in the same place.
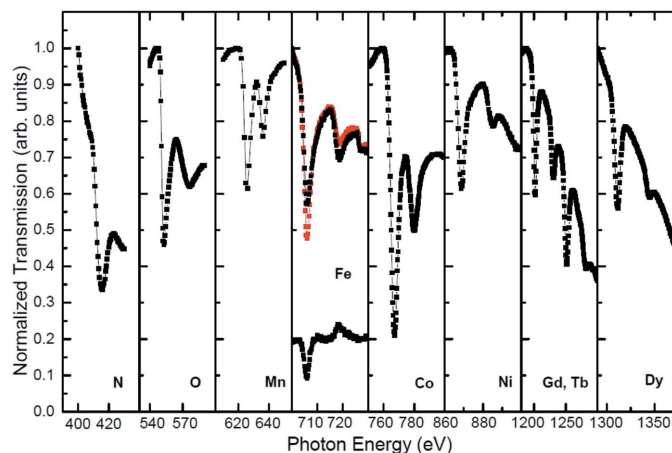
Figure 10
Transmittance spectra taken from different thin films on Si_3N_4 containing the elements of interest in the corresponding spectral range as defined by the individual lenses. In the Fe lens case an XMCD example at the L-edges is plotted. The red and black curves correspond to the two magnetization directions and the lower curve is the resulting magnetic asymmetry in usual magnetic asymmetry units (0.1/div on the outermost the left axis).

$$\Delta h_{\mathrm{odd}} = \frac{2R_2' hc}{NEd(E)\sin\beta} = \text{a constant}, \qquad (11)$$

a value that no longer depends on E since the line density d is proportional to $1/E$ according to equation (6). These images indicate that a focal plane array detector of certain pixel size equally performs at the same $E/\Delta E$ for all lenses (except Fe 2000), albeit this is valuable only in a very limited energy range around the design energy according to Fig. 4. Finally, the spectral characterization of the RZPA's spectral capabilities was made using pitch sweeps and a GaAsP diode right behind a 20 µm exit slit. Fig. 10 shows this sort of photon energy scan as performed employing BESSY II's generic monochromator hardware and software (Follath & Balzer, 2013). All initially envisaged absorption edges can be addressed as well as transitions that lie within margins of 5% around the central energies according to Table 3, albeit at slightly reduced spectral resolution (see Fig. 4).

8. Summary and conclusions

We have successfully designed, built and commissioned a novel type of high-flux monochromator beamline for ultrafast applications that is based on an array of off-axis reflection zone plates (RZPAs). The current optics consisting of nine RZPs covers the soft X-ray range from 410 to 1333 eV at moderate resolution of $E/\Delta E = 500$ and minimum pulse elongation of 30 fs. It was also shown that a higher resolution of $E/\Delta E = 2000$ can be achieved with higher line density, albeit at the expense of a temporal elongation of 120 fs. As the new beamline consists only of a single optical element, its transmittance is up to 21%. The beamline went into regular user operation in November 2012 and has been proven to perform as expected supporting optical pump–X-ray probe experiments at 6 kHz duty cycle and at time resolutions of ∼100 fs

(slicing), <10 ps (in low-α mode) and <100 ps (in regular user mode). We can state that RZPAs are well suited for time-resolved XMCD, time-resolved XAS and resonant soft X-ray diffraction applications with slicing and HHG sources in the soft X-ray range.

APPENDIX *A*
Fabrication of reflection zone-plate arrays

After defining the number and parameters of the individual lenses, their structure was calculated using an efficient software package that has been specifically developed for structural design and simulation of imaging properties of diffractive optics at Institut für Nanometeroptik und Technologie (INT) at HZB in close collaboration with the Institute of Microelectronics Technology and High Purity Materials (RAS, Chernogolovka, Russia) (see Firsov *et al.*, 2013).

Thickness profiles, source properties as well as substrate properties like slope errors and roughness have been accordingly considered. The resulting RZP structure was used as input for the *Nanomaker* software (Interface Ltd) that finally produced proper input files for optical lithography, mask design and fabrication. The current RZPA was produced in the technological facilities of HZB's INT. Lithography masks made by e-beam writing were provided by Compu-
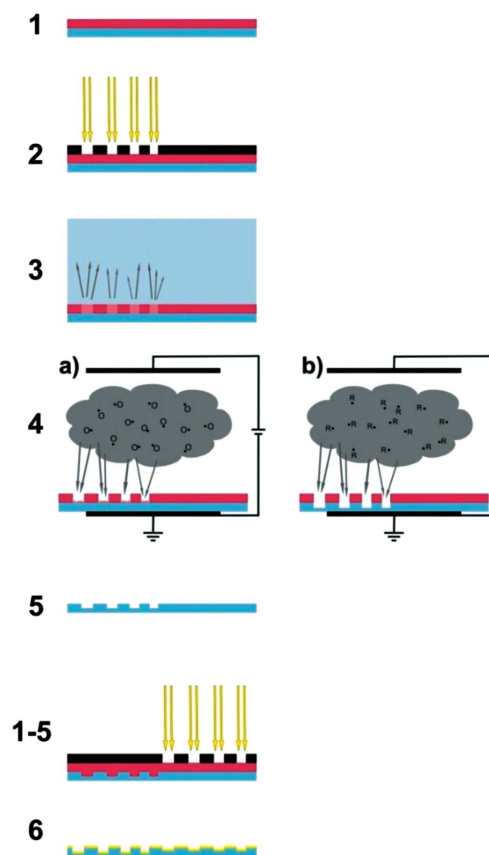

Figure 11
Diagram of stages of manufacturing of RZPAs. A variable groove depth for the two lens groups is realised by different local etching procedures (with masks) in step #4.

graphics Jena GmbH. As depicted in Fig. 11, starting with a plane super-polished silicon substrate of 10 mm thickness, a positive photosensitive resist (AZ701 MIR, Allresist GmbH) was spin-coated onto the surface (step 1) and patterned by UV photolithography with five low-energy RZP lenses using a first mask (step 2). The exposed resist is subsequently developed in an organic solution (AR600-56, Allresist GmbH) (step 3). In following reactive ion etching procedures, residual developer and resist were firstly removed from the grooves and, secondly, the structures of five lenses were formed into the silicon substrate (step 4). Afterwards, residual resist was removed by cleaning in acetone (step 5). Steps 1–5 were repeated for mask 2. Finally, the cleaned substrate is coated by a magnetron sputtering technique with 60 nm gold (step 6). The lenses as manufactured (see image in Fig. 2) were characterized by secondary electron microscopy (SEM, LEO 1560), atomic force microscopy (AFM) and with a white-light interferometer, in all cases at nanometer accuracy. The minimum zone size of the lens was measured to be 780 nm, *i.e.* close to the design value. A maximum deviation between design parameters and measured dimensions of less than 20 nm was found. The surface roughness as measured by AFM was determined to be less than 1 Å (r.m.s.) over the whole lens area.

References

Aristov, V. V., Erko, A. I. & Martynov, V. V. (1988). *Rev. Phys. Appl. (Paris)*, **23**, 1623–1630.

Bahrdt, J. (2012). *Undulatoren*, http://www.helmholtz-berlin.de/forschung/grossgeraete/undulatoren/.

Basov, Yu. A., Roshchupkin, D. V. & Yakshin, A. E. (1994). *Opt. Commun.* **109**, 324–327.

Boeglin, C., Beaurepaire, E., Halté, V., López-Flores, V., Stamm, C., Pontius, N., Dürr, H. A. & Bigot, J. Y. (2010). *Nature (London)*, **465**, 458–461.

Erko, A., Firsov, A. & Holldack, K. (2010). *AIP Conf. Proc.* **1234**, 177–180.

Erko, A., Firsov, A., Roshchoupkin, D. & Schelokov, I. (2008). *Modern Developments in X-ray and Neutron Optics*, edited by A. Erko, M. Idir, T. Krist and A. G. Michette, pp. 471–500, *Springer Series in Optical Sciences*, Vol. 137. Berlin/Heidelberg: Springer.

Eschenlohr, A., Battiato, M., Maldonado, P., Pontius, N., Kachel, T., Holldack, K., Mitzner, R., Föhlisch, A., Oppeneer, P. M. & Stamm, C. (2013). *Nat. Mater.* **12**, 332–336.

FEMTOSPEX (2013). *A versatile optical pump–X-ray probe facility at BESSY II.* In preparation.

Firsov, A., Brzhezinskaya, M., Svintsov, A. & Erko, A. (2013). *J. Phys.* **425**, 162004.

Follath, R. & Balzer, A. (2013). Private communication.

Gavrila, G., Godehusen, K., Weniger, C., Nibbering, E. T. J., Elsaesser, T., Eberhardt, W. & Wernet, P. (2009). *Appl. Phys. A*, **96**, 11–18.

Heimann, P. A., Glove, T. E., Plate, D., Lee, H. J., Brown, V. C., Padmore, H. A. & Schoenlein, R. W. (2006). *AIP Conf. Proc.* **879**, 1195–1197.

Holldack, K., Kachel, T., Khan, S., Mitzner, R. & Quast, T. (2005). *Phys. Rev. ST Accel. Beams*, **8**, 040704.

Holldack, K., Pontius, N., Schierle, E., Kachel, T., Soltwisch, V., Mitzner, R., Quast, T., Springholz, G. & Weschke, E. (2010). *Appl. Phys. Lett.* **97**, 062502.

Ingold, G., Beaud, P., Johnson, S. L., Grolimund, D., Schlott, V., Schmidt, T. & Streun, A. (2007). *Synchrotron Radiat. News*, **20**, 35.

Kachel, T., Holldack, K., Khan, S., Mitzner, R., Quast, T., Stamm, C. & Dürr, H. A. (2007). *AIP Conf. Proc.* **879**, 1250.

Khan, S., Holldack, K., Kachel, T., Mitzner, R. & Quast, T. (2006). *Phys. Rev. Lett.* **97**, 074801.

Kuske, P. (2013). Private communication.

Niemann, B. (1995). Deutsches Patent DE 195 42 679 A1, 16.11.

Popmintchev, T., Chen, M.-C., Arpin, P., Murnane, M. M. & Kapteyn, H. C. (2010). *Nat. Photon.* **4**, 822-832.

Radu, I., Vahaplar, K., Stamm, C., Kachel, T., Pontius, N., Dürr, H. A., Ostler, T. A., Barker, J., Evans, R. F., Chantrell, R. W., Tsukamoto, A., Itoh, A., Kirilyuk, A., Rasing, T. & Kimel, A. V. (2011). *Nature (London)*, **472**, 205–208.

Schäfers, F. (2008). *The BESSY Raytrace Program RAY* in *Modern Developments in X-ray and Neutron Optics*, edited by A. Erko, M. Idir, T. Krist and A. G. Michette, pp. 471–500, *Springer Series in Optical Sciences*, Vol. 137. Berlin/Heidelberg: Springer.

Schäfers, F. & Krumrey, M. (1996). BESSY Technical Report 1996, p. 201. BESSY, Germany.

Schoenlein, R. W., Chattopadhyay, S., Chong, H. H. W., Glover, T. E., Heimann, P. A., Shank, C. V., Zholents, A. A. & Zolotorev, M. S. (2000). *Science*, **274**, 236.

Siewert, F. (2013). Private communication.

Stamm, C., Kachel, T., Pontius, N., Mitzner, R., Quast, T., Holldack, K., Khan, S., Lupulescu, C., Aziz, E. F., Wietstruk, M., Dürr, H. A. & Eberhardt, W. (2007). *Nat. Mater.* **6**, 740–743.

Warwick, T., Heimann, P., Mossessian, D., McKinney, W. & Padmore, H. (1995). *Rev. Sci. Instrum.* **66**, 2037.

Weiss, M. R., Follath, R., Sawhney, K. J. S., Senf, F., Bahrdt, J., Frentrup, W., Gaupp, A., Sasaki, S., Scheer, M., Mertins, H.-C., Abramsohn, D., Schäfers, F., Kuch, W. & Mahler, W. (2001). *Nucl. Instrum. Methods Phys. Res. A*, **467–468**, 449–452.

Wiedemann, H. (1998). *Particle Accelerator Physics II*, p. 425. Berlin: Springer.

Wietstruk, M., Melnikov, A., Stamm, C., Kachel, T., Pontius, N., Sultan, M., Gahl, C., Weinelt, M., Dürr, H. A. & Bovensiepen, U. (2011). *Phys. Rev. Lett.* **106**, 127401.

Wilhein, T., Hambach, D., Niemann, B., Berglund, M., Rymell, L. & Hertz, H. M. (1997). *Appl. Phys. Lett.* **71**, 190.

Woodruff, D. P. (1995). *J. Synchrotron Rad.* **2**, 276–287.

Yu, L. H. (1991). *Phys. Rev. A*, **44**, 5178–5193.